13th International Symposium on Particle Image Velocimetry – ISPIV 2019
Munich, Germany, July 22-24, 2019

Volumetric Microscopic Flow Measurement with a Stereoscopic Micro-PIV System

Christina Hesseling[1*], Lutz Fiedler[1], Douglas R. Neal[2], Dirk Michaelis[1]

[1] LaVision GmbH, Anna-Vandenhoeck-Ring 19, D-37081 Göttingen, Germany

[2] LaVision Inc., 211 W. Michigan Ave., Suite 100, Ypsilanti, MI 48197, USA

[*] chesseling@lavision.de

Abstract

3D flow measurement at microscale requires a high spatial resolution to properly resolve the details of interest (boundary layer, near wall region etc.). This demand is combined with a strongly limited optical access making 3D microscale flow measurements a particular challenge. The particle tracking method Shake-the-Box and tomographic PIV using 3D cross-correlation usually rely on recordings by at least three cameras, typically forming a viewing angle not accessible in Micro-PIV. A standard stereoscopic Micro-PIV system uses two cameras in a small stereo angle. This paper presents how the data from such a system can be used for 3D microflow measurement with tomographic PIV or Shake-the-Box. Shake-the-Box particle tracks are converted to a regular grid using data binning and using data assimilation. Tomographic PIV and Shake-the-Box are compared using identical measurement data of the flow over a backward-facing step from 50 µm to 100 µm depth. Average and instantaneous flow fields are compared demonstrating that Shake-the-Box is a feasible method for volumetric microflow measurement. The expected parabolic flow profile in depth direction cannot be resolved by the coarse grid data retrieved with tomographic PIV, whereas it is reconstructed with Shake-the-Box. After conversion to a regular grid, also time-averaged pressure fields can be retrieved.

1 Introduction

Due to the low Reynold numbers common in microfluidics, these flows are usually laminar. Still, strong surface effects and forces, which are neglectable for most macroscopic flows, make these flows complicated [Raffel et al. (2018)], whereas their wide application range, e.g. in life sciences, motivate the experimental investigation of continuum microfluidic flows in a volume.

Usually, three dimensional flow measurements with Shake-the-Box (STB) [Schanz et al. (2016)] or tomographic PIV (Tomo-PIV) [Elsinga et al. (2006)] rely on the recording of particle images from multiple angles by at least three cameras, preferably by four at minimum. This cannot be achieved by standard microscopic systems. Instead, a stereoscopic microscope delivers two views of the sample. How these two views can be exploited either by correlation-based Tomo-PIV or by the particle tracking algorithm STB and how the results of these two techniques compare for a backward-facing step are the subjects of the current paper.

2 Experimental Setup

A photo of the experimental setup used in this study is shown in figure 1 (a), though for the experiment presented here different cameras, two Phantom VEO 710L, are used. The optical components are a Zeiss Stereo Lumar microscope with a 1.5× objective lens, camera adapters, two ≥ 540 nm long-pass filters, and a Photonics Industries DM-30 laser, which is coupled via a laser coupler into an optical fiber connected to the fluorescence stereo microscope having a separate beam path for the laser illumination. The total magnification of the system is 4.65×. The water flow in a demo micro channel is seeded with 7 µm Rh6G dyed PS particles and driven with a syringe pump Chemyx Fusion 200. The whole system is controlled

from a Windows PC using the software DaVis 10 and LaVision's Programmable Timing Unit (PTU X) for highspeed applications.

In the microscope the same objective lens is used for co-axial illumination and recording by both cameras. A setup with one common main objective lens provides the benefit of a maximized image and focus overlap, whereas it introduces asymmetric image distortions for the two cameras [Cierpka and Kähler (2012)].

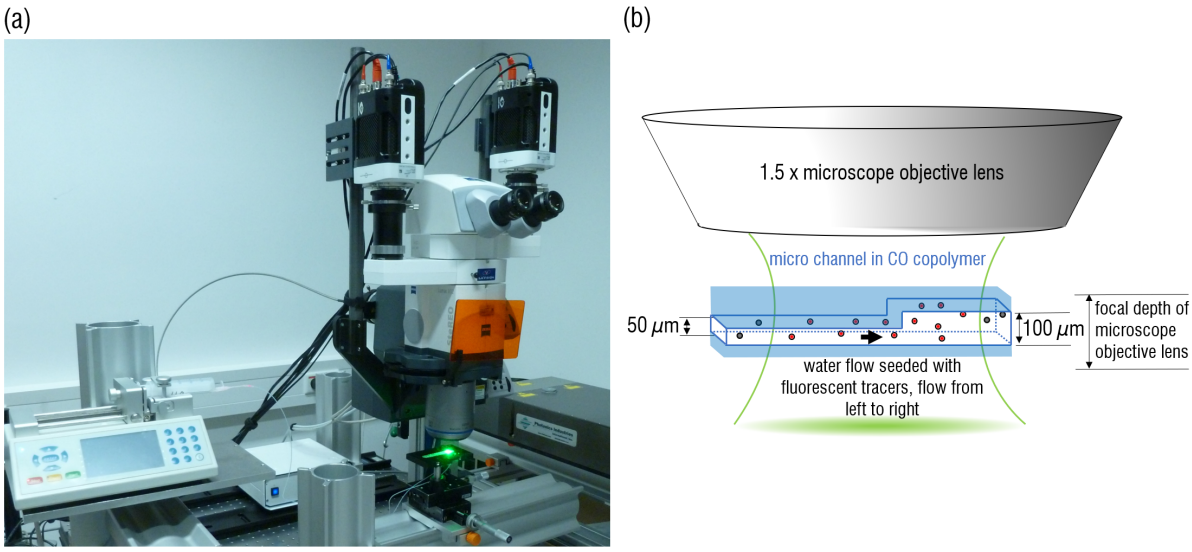

Figure 1: (a) System setup for tomographic µ-PIV and µ-Shake-the-Box. (b) Sketch of the measurement section.

Polystyrene seeding particles dyed with rhodamine 6G are used, which emit a red fluorescence signal when illuminated by green light at the wavelength 527 nm. The two long-pass filters (transmission ≥ 540 nm) block the illuminating laser light while transmitting the red signal from the particles. This greatly reduces background stray light.

The micro channel is placed inside the focal depth of the microscope objective lens, as sketched in figure 1 (b). In this way, the particle fluorescence signal is not blurred by defocussing over the depth of the micro channel and can be evaluated in the entire volume. This approach avoids the depth of correlation (DOC) problem inherent to planar µ-PIV, where the signal in the plane of interest is always influenced by particles outside this plane due to the volumetric illumination [Cierpka and Kähler (2012)].

3 Backward-facing Step in a Micro Channel

The flow over a backward-facing step is recorded at 4 kHz over 1000 images, i.e. for 0.25 s. The respective test section in the micro channel made of CO copolymer is marked in red in figure 2. The channel width is 1.5 mm, and the recorded length of the section is approximately 3 mm, whereas the height of the channel changes from 50 µm to 100 µm in a step. According to numerical and experimental studies [Cierpka and Kähler (2012)] from a backward facing step, two main flow features can be expected: first, the downflow on the step, second, a parabolic flow profile in the out-of-plane direction, i.e. in z, in the sections with constant height.

4 Calibration

The calibration procedure in µ-PIV, i.e. finding the mapping function between the volume of interest and the camera images, is challenging since the calibration target can usually not be placed inside the volume of interest. Therefore, the calibration is performed in two steps. First, a calibration based on a calibration target is performed. Second, after the recording of particle images, volume self-calibration [Wieneke (2008, 2018)] is applied.

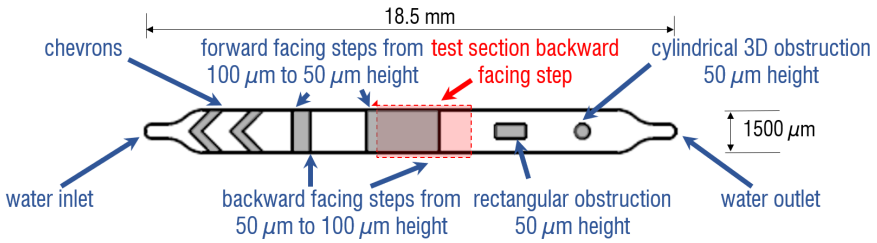

Figure 2: Sketch of the micro channel with the used test section marked in red. The channel height is 100 µm. Obstructions reducing the channel height to 50 µm are shown in gray. The width of the channel is 1500 µm.

The planar calibration target, figure 3 (b), has a horizontal and vertical marker distance of 20 µm. For the calibration, the target takes the place of the micro channel, as sketched in figure 3 (a). Underneath the calibration plate a red fluorescent plate (Perspex Fluorescent) is positioned so that the markers show up as dark spots before a red background. This means the long pass filters that protect the camera sensors from green (and most of the ambient) light stay in place during the calibration recordings, and the calibration is performed with laser illumination. For the calibration, two images are recorded with both cameras, with the calibration plate traversed, e.g. by 50 µm, in the out-of-plane direction, here referred to as z-direction. This yields recordings of two parallel planes at a known z-displacement. For the mapping between camera images and sample volume, the markers are automatically detected in DaVis and polynomials are fit to the markers in both planes. Since the actual measurement will take place in water and not in air, a distance of 50 µm between two recorded positions of the calibration plate is mapped to a distance of 1.33·0.05 mm = 0.0665 mm in the calibration with $\frac{n_{water}}{n_{air}} \approx \frac{1.33}{1.0}$ being the ratio of the refractive indices of water and of air.

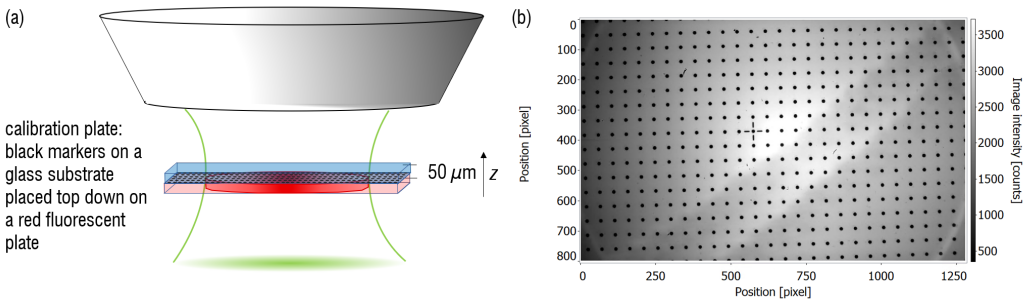

Figure 3: (a) Sketch of the calibration process. (b) Image recorded by camera 1 for one plate position.

Although the difference between the refractive indices of water and air is taken into account in this calibration, possible optical distortions introduced by the additional polymer layer in the measurement are not yet included in the calibration. These optical distortions may have a significant effect due to the high magnification in this application. A low calibration error is imperative to ensure the quality of Tomo-PIV and STB measurements. Therefore, in addition to the initial calibration, volume self-calibration is performed, which takes the particle images themselves as basis for the correction [Wieneke (2008, 2018)].

5 Image Preprocessing

A raw camera image is shown in figure 4 (a). Each camera sensor has a full resolution of 1280×800 px. The image of the micro channel covers approximately 28 % of these pixels. The fluorescence signal is scattered by the micro channel, which is therefore visible despite the long-pass filters. Also, four large (in addition to numerous smaller) air bubbles are visible in the channel with particles sticking to the air-water interfaces.

To optimize the signal quality, the images are preprocessed. As only the signals changing with time are relevant, first, the temporal average over 1000 time steps is subtracted from each image in the sequence. A

mask is introduced which keeps only the inner part with the channel for the evaluation. The result is shown in figure 4 (b). Now the signal generated by the bubbles is nearly completely removed showing black areas at their positions and no further image preprocessing is executed for the STB evaluation presented below. For Tomo-PIV analysis, the biggest bubbles are masked by a geometric mask generated by polygons. The result is shown in subfigure (c).

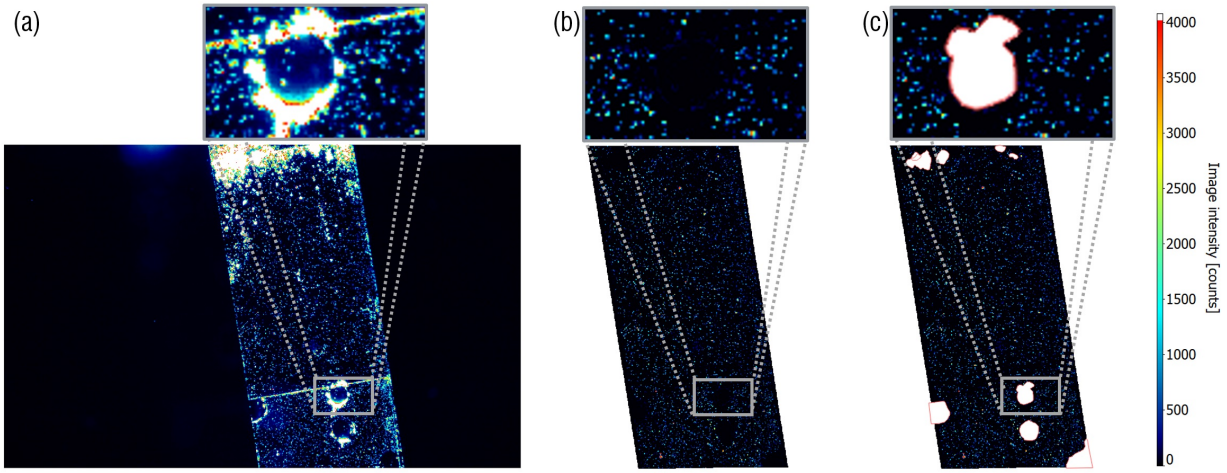

Figure 4: Image recorded by one camera: (a) raw image (b) image preprocessed by subtraction of the average over all time steps and masking (c) preprocessing for Tomo-PIV by geometric masking of the biggest air bubbles.

6 Methods for 3D Flow Analysis

The same 1000 images recorded at 4 kHz together with the calibration mapping are analyzed by Tomo-PIV and STB.

6.1 Tomographic PIV: Cross Correlation of 3D Intensity Fields

The particle images are analyzed by the well-known method Tomo-PIV [Elsinga et al. (2006)]. In contrast to particle tracking methods, Tomo-PIV reconstructs a volume in the region of interest for each time step and retrieves the velocity information from cross-correlating reconstructed subvolumes. Each volume is reconstructed with Sequential Motion Tracking Enhancement (SMTE) [Lynch and Scarano (2015)] using six MART iterations [Elsinga et al. (2006)] and multi-pass cross-correlation from the interrogation volume size $96 \times 96 \times 96$ vox down to $20 \times 20 \times 20$ vox (for time-averaged results down to $8 \times 8 \times 8$ vox), in 10 passes in total with an overlap of 75 %. Universal outlier detection is applied between the passes [Westerweel and Scarano (2005)] but not after the final pass. Between the passes, the vector field is smoothed with 2^{nd} order polynomial fits using the adjacent vectors. The sizes of the regions for the smoothing and for outlier detection, from now on referred to as filter, are defined equal. To minimize the influence by the data gaps caused by air bubbles, additional masks as shown in figure 4 (c) are applied. Also a mask in the *yz*-plane is applied, to mask the copolymer of the channel where the channel height is only 50 µm.

6.2 Shake-the-Box: Lagrangian Particle Tracking

STB tracks individual particles over time in 3D. The shapes of particle images are carefully taken into account, since they can change severely with the particle position in the volume. This is reflected in the optical transfer function (OTF) [Schanz et al. (2012)] evaluated for the current experimental situation. The OTF reflects effects by the optical system on the imaging of a particle individually for each camera. In this way, asymmetrical distortions due to the non-central view through the common main objective of the stereoscopic microscope are taken into account by STB.

Particle tracking is performed by STB [Schanz et al. (2016)] in DaVis 10 with the length of four time-steps for the 2nd order polynomial functions used to fit particle tracks for the prediction of particle positions in the next time step. For the experiment presented here, in average more than 7900 particles are tracked over 1000 time steps, which corresponds to a seeding density of approximately 0.03 ppp. Second order polynomials are fit to the track data over ± 2 time steps to retrieve velocity and acceleration data for each particle position.

For time steps 100 ± 3, the resulting tracks color coded by the velocity magnitude are shown in figure 5. It is clearly visible that the particles are accelerated at the step and by the obstacles caused by the air bubbles, which add complexity to the flow field. Although no additional track filter is applied to this data, very few outliers are visible.

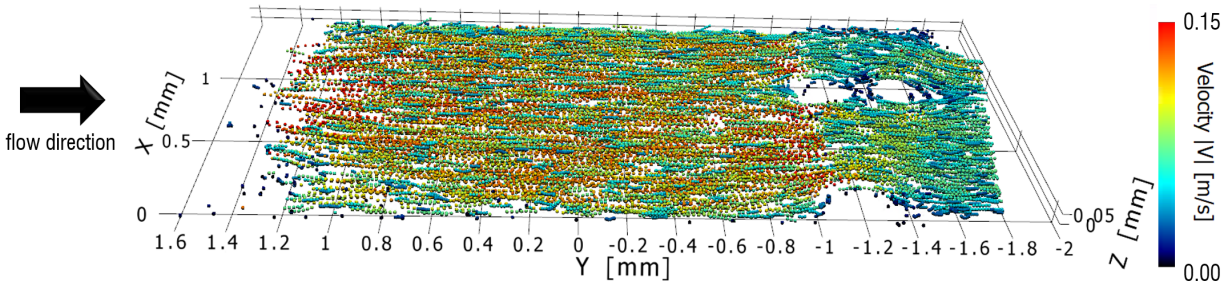

Figure 5: Particle tracks in seven time steps color coded by velocity magnitude retrieved from 2nd order polynomial fits over five time steps.

Finally, the particle tracks are converted to a regular grid. Here, either binning can be used or data assimilation. The parameters for each method are described briefly in the following sections.

6.2.1 Data binning for time-averaged and instantaneous data

In data binning, the bin size is selected between 20 and 4 vox per dimension and the overlap is fixed to 75 %. This yields a final grid resolution between 5 and 1 vox. The distance of a particle to a bin determines its influence on this bin. For the time-resolved results shown below, Gaussian weighting is used to define the bins. If no particle is present inside a bin, this bin will be ignored. Due to the larger data basis for time-averaged results, here, at least five particles have to be present in one bin and polynomial regression of 2nd order is applied [Agüera et al. (2016)].

6.2.2 Data assimilation for instantaneous data at high resolution

For time-resolved results, a second analysis of the STB-tracks is performed based on data assimilation. Here the method Fine Scale Reconstruction (FSR), also referred to as VIC#, is employed [Jeon et al. (2019)], which evolved from Vortex-in-Cell+ (VIC+) [Schneiders and Scarano (2016)]. To minimize the influence of noise, only tracks with a minimum length of five time steps are taken into account, and the range of the investigated volume is reduced to $y \in [-1.7, 1]$ mm. Unlike approaches using data binning, FSR retrieves data for the whole volume independent of the existence of a particle track in a subvolumes. Therefore, data gaps are filled by data fulfilling physical constraints but also sections are filled with data, which are actually not covered by the flow field. Hence, finally, a mask in the yz-plane is applied to exclude the volume of the layer of the copolymer before the backward-facing step. The final grid resolution is set to 5 vox.

7 Analysis of Instantaneous Vector Fields

The track data are binned with bin sizes of $20 \times 20 \times 20$ vox with 75 % overlap, i.e. the final grid resolution is 5 vox in each dimension with 75×175 vectors in six planes, whereas the data shows gaps where no particle track is detected. The result for time step 100 of the 1000 recorded images is shown in figure 6.

Clearly, the positions of the air bubbles in the micro channel can be seen as gaps in the data. Also the position of the step is clearly visible, especially in the v-component, which noticeably drops here as

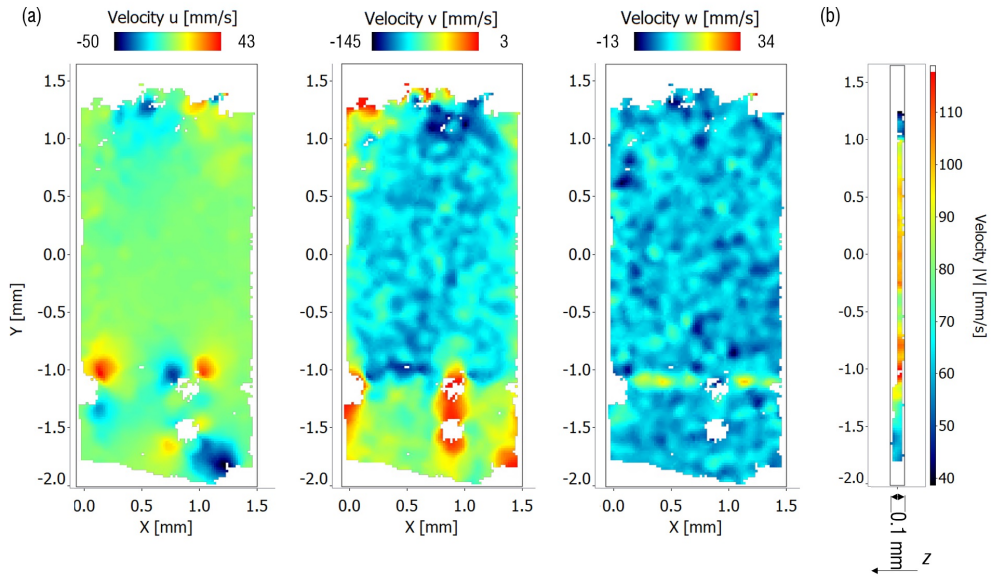

Figure 6: (a) Three components of the instantaneous velocity field on a grid retrieved from STB particle tracks by binning with Gaussian weighting for a bin size of $20 \times 20 \times 20$ vox with 75 % overlap in plane $z \approx -0.01$ mm. (b) Velocity magnitude in the yz-plane at $x \approx 0.25$ mm.

expected, whereas w shows a peak at the step. Also the influence of the air bubbles on the flow field is observed, which increases the magnitude of the u component, which otherwise is close to zero because of the channel symmetry. Due to the flow compression in the region of the bubbles, the v component increases here.

Although many flow features are visible in figure 6, there are still data gaps even with a single particle regarded as sufficient to define a bin. Also the expected parabolic profile in the v-component is not visible in the plane shown in figure 6 (b). Therefore, FSR is executed inside a volume of $373 \times 645 \times 27$ vox $\approx$ $1.562 \times 2.7 \times 0.113$ mm. The result for time step 100 is shown in figure 7. Figures (a) and (b) both show the v-component in multiple yz-planes in the reconstructed volume but with different velocity scales. Figure (b) clearly shows that in the sections of the large data gaps, e.g. due to the air bubbles, the v-velocity component is mainly filled up with values ≥ 0 m/s, which are hardly present in the result based on data binning and probably unphysical. On the other hand, the remaining vector field with $v < 0$ m/s shows that a first indication of a parabolic profile is visible.

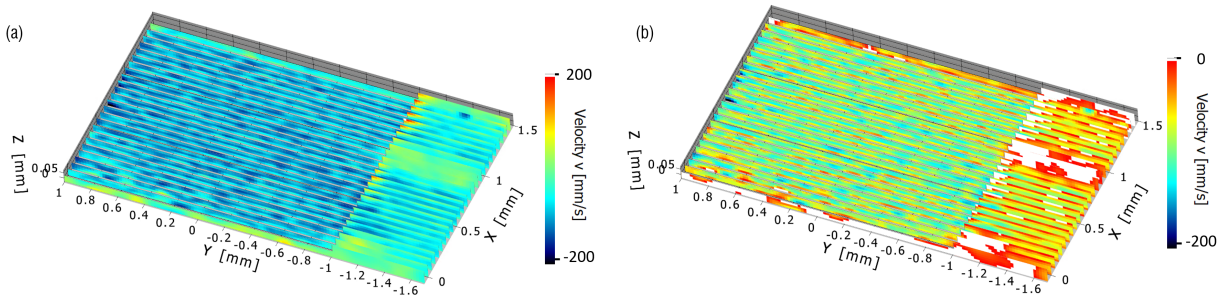

Figure 7: Instantaneous result retrieved by Fine Scale Reconstruction down to a resolution of $5 \times 5 \times 5$ vox with 1 vox $\approx 4\,\mu$m. Every 3$^{\text{rd}}$ yz-plane is shown.

Also Tomo-PIV is performed on the data for the two filter sizes $3 \times 3 \times 3$ and $5 \times 5 \times 5$ vectors. Two different filter sizes are applied here to check whether they influence the smoothing effect which can be expected from correlation-based techniques due to the finite correlation window size [Cierpka and Kähler (2012)]. For comparison, four profiles of the velocity component v are retrieved for four different y positions along the channel at $x \approx 0.25$ mm, which is a position where no large air bubble blocks the channel. Figure 8 displays the profiles and a sketch visualizing the positions of the profiles in the channel. Black lines mark the approximate positions of the channel walls, which are reconstructed from the time-averaged result of STB tracks converted to a grid by $8 \times 8 \times 8$ vox binning, shown in figure 11. It is difficult to estimate wall locations from velocity profiles near the wall [Kähler et al. (2012b)]. Therefore, the data points in the centre of the channel are used for this estimate. In figure 8 Tomo-PIV shows nearly the same results independent of the filter size. Before the step, Tomo-PIV and binning resolve only two z-planes. Hence, no profile can be expected. The three data points of FSR indicate a first idea of a parabolic profile, but the data basis is still too small. Behind the step, between four and six z-planes are reconstructed. The results of Tomo-PIV and binning remain close to constant with z, whereas FSR shows a dip in all three cases.

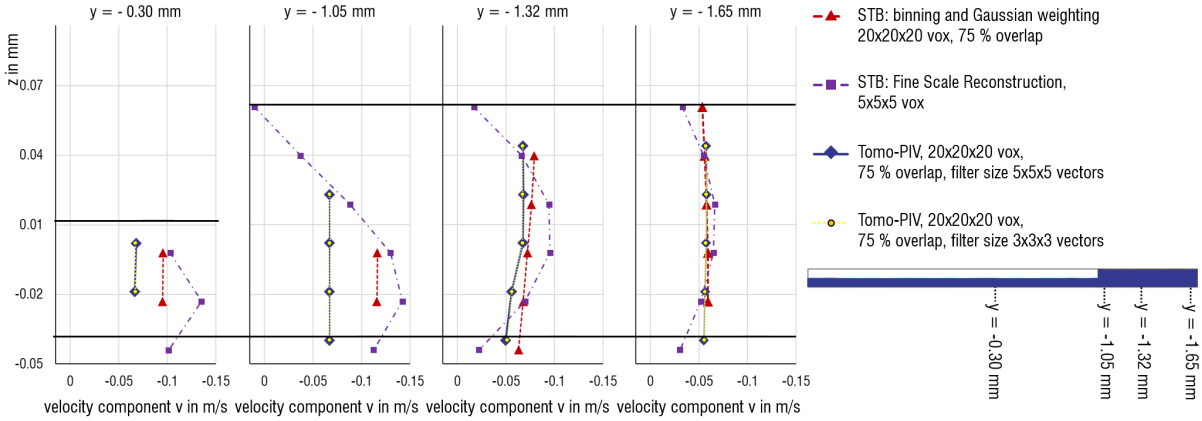

Figure 8: Profiles of the v velocity component at four y-positions $x \approx 0.25$ mm retrieved from the same time step as shown in figures 6 and 7 for two evaluations from STB particle tracks and two Tomo-PIV results. Black horizontal lines mark the approximate channel borders.

8 Analysis of Temporal Averages

Though the instantaneous results give an initial view of the flow phenomena, the data remain noisy in space and time. Therefore, the temporal averages over all 1000 time steps are retrieved by Tomo-PIV and by binning of STB tracks combined with 2$^{\text{nd}}$ order polynomial regression [Agüera et al. (2016)]. Here, the spatial grid resolution is increased as the information is accumulated over time. So bin sizes of $8 \times 8 \times 8$ vox and $4 \times 4 \times 4$ vox are set for binning. As before, 75 % overlap is used. Hence, the final grid resolutions are increased by a factor of four in each dimension compared to bin size. For $4 \times 4 \times 4$ px bins from STB tracks, this yields a vector field with 374×873 vectors in 28 z-planes with valid vectors for bins with at least five tracked particles. For Tomo-PIV, $8 \times 8 \times 8$ vox is the final interrogation window size yielding a vector grid resolution of $2 \times 2 \times 2$ vox. Here, the reconstructed volume is $373 \times 873 \times 26$ vox $\approx 1.56 \times 365 \times 0.11$ mm^3.

Figure 9 displays the result from STB-tracks (a) and Tomo-PIV (b) of the velocity magnitude. Taking the different color scales into account, the smoothing by the correlation window in Tomo-PIV is clearly visible. Together with the results from the $4 \times 4 \times 4$ vox binning of STB-tracks, the yz-planes at $x \approx 0.26$ mm are visible in figure 10. Clearly, the parabolic profiles show up behind the step in all results. A closer look at four profiles, displayed in figure 11 for four different positions in the channel, shows that Tomo-PIV and STB perform nearly equal far behind the step, whereas close to the step and in the thinner region before the step, STB shows the parabolic profile more clearly, especially at higher grid resolution. The filter length (three or five vectors) in Tomo-PIV shows no decisive effect.

Finally, also the time-averaged relative pressure is retrieved from the data shown in 9 (a) [Jeon et al. (2017)]. The result for $z \approx -0.01$ mm is shown in figure 12 together with two line plots. Clearly, the

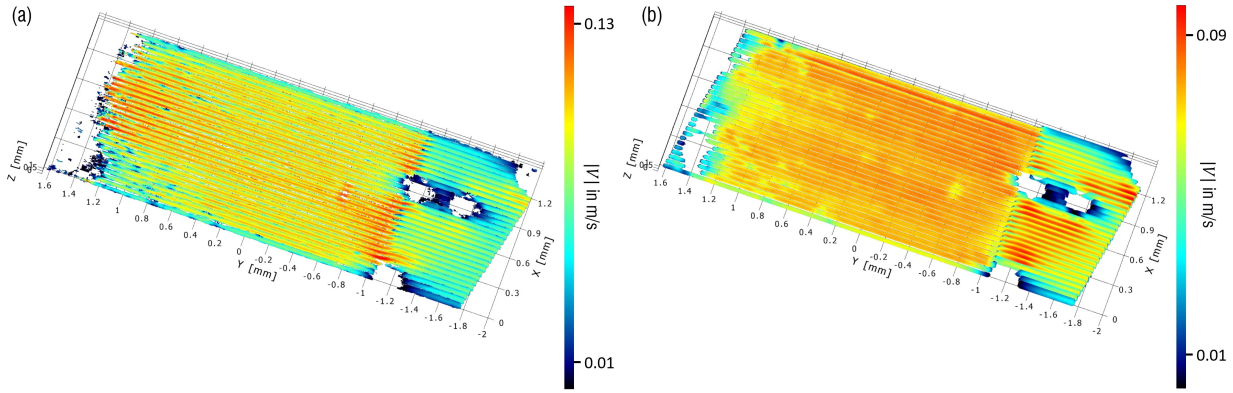

Figure 9: Every 6$^{\text{th}}$ yz-plane of the velocity magnitude time-averaged from 1000 images. (a) Tracks are converted to a grid by binning and polynomial regression with a bin size of $8 \times 8 \times 8$ vox with 75 % overlap. (b) Tomo-PIV evaluation is executed with a final interrogation window size of $8 \times 8 \times 8$ vox at 75 % overlap and a filter size of $5 \times 5 \times 5$ vectors.

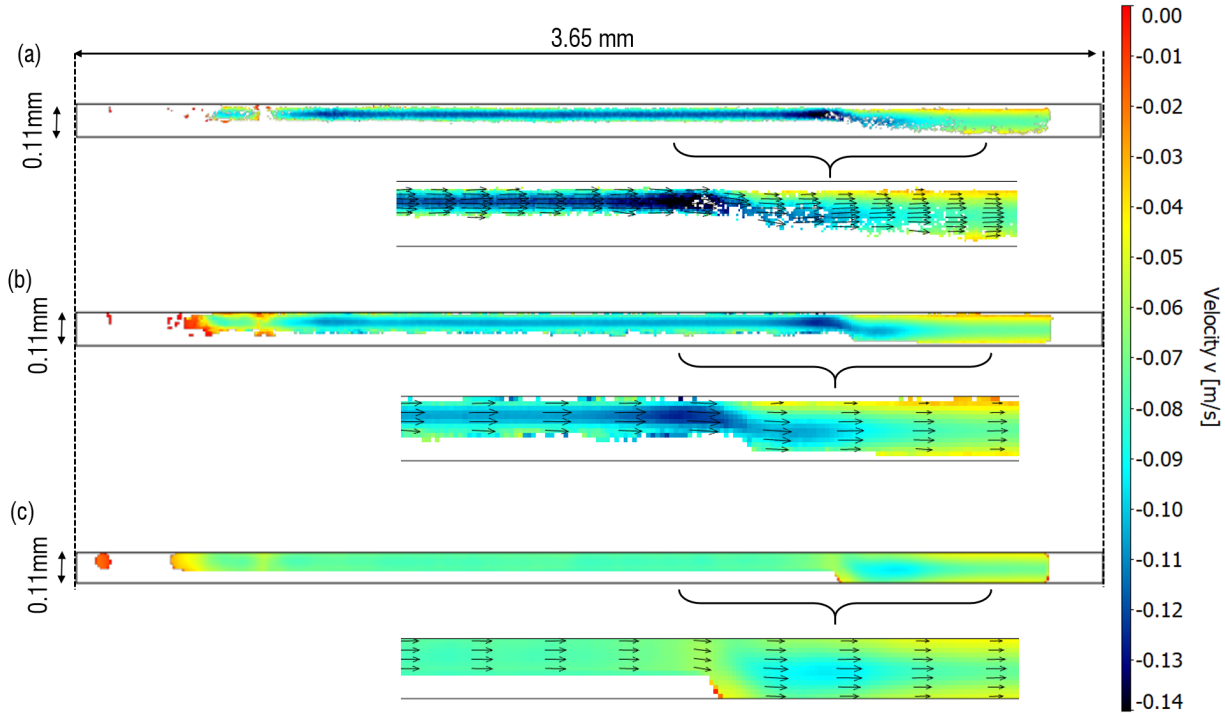

Figure 10: Plane cuts through STB and Tomo-PIV results that are time-averaged from 1000 images at $x \approx 0.26$ mm. In the zoomed sections every 16$^{\text{th}}$ horizontal and every 2$^{\text{nd}}$ vertical vector is shown. (a) Tracks are converted to a regular grid by binning and polynomial regression with a bin size of $4 \times 4 \times 4$ vox with 75 % overlap. (b) Tracks are converted to a grid by binning and polynomial regression with a bin size of $8 \times 8 \times 8$ vox with 75 % overlap. (c) Tomo-PIV evaluation is executed with a final interrogation window size of $8 \times 8 \times 8$ vox at 75 % overlap and a filter over $5 \times 5 \times 5$ vectors.

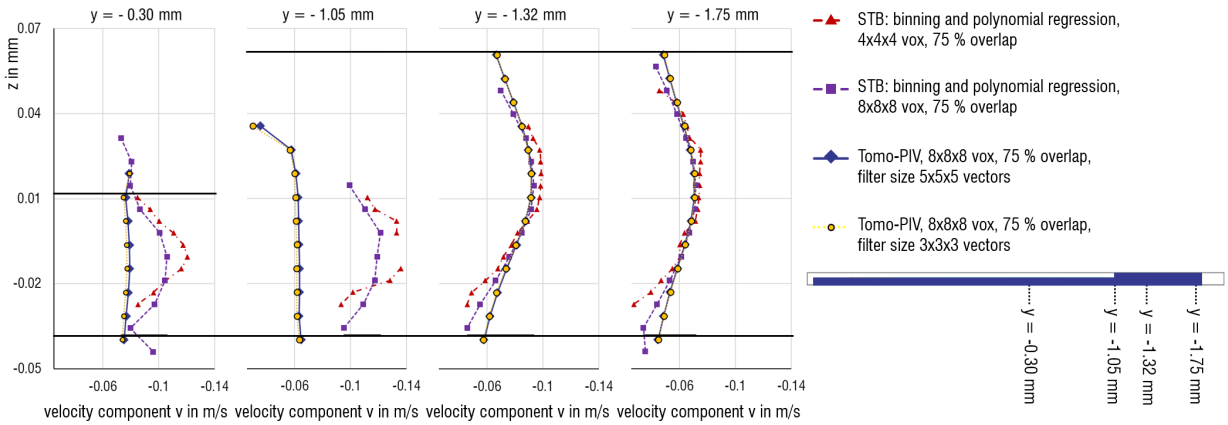

Figure 11: Profiles of the temporal average of the v velocity component at four y-positions for the planes displayed in figure 10 at $x \approx 0.26\,\text{mm}$. Right the positions in the channel are visualized. Black horizontal lines mark the approximate channel borders.

pressure gradient drops at the step position. In the second profile (black) also a small pressure increase is observed when the flow approaches a bubble.

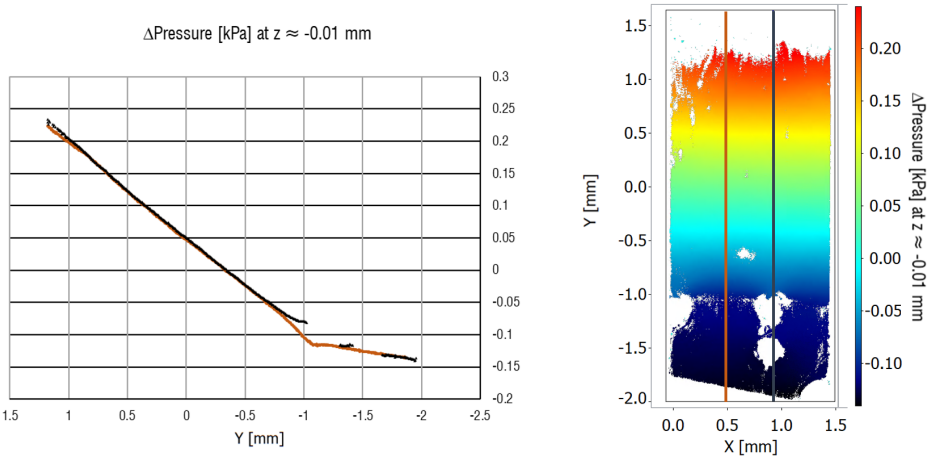

Figure 12: Time-averaged relative pressure over 1000 time steps from Shake-the-Box particle tracks converted to a regular grid using 2$^{\text{nd}}$ order polynomial regression with bin size $4 \times 4 \times 4$ voxel with 75 % overlap. Data points are regarded as valid if at least five particles are found in the respective bin.

9 Conclusion

This paper presents results of Tomo-PIV and STB combined with two approaches for conversion of particle track data to a regular grid for the special case of microflow measurement. To retrieve these 3D results a standard fluorescence stereo microscope was used. The application example of a backward facing step shows that 3D flow measurements at microscale can be performed with STB and Tomo-PIV. A smoothing effect can be expected from techniques using finite correlation window sizes [Kähler et al. (2012b); Cierpka and Kähler (2012)]. This is confirmed in this study showing a lower spatial resolution for Tomo-PIV than for STB results. Here, the two methods data binning and data assimilation are used for conversion of particle tracks to a regular grid for instantaneous data. Although first promising results could be seen based on data assimilation, the correct treatment of boundaries remains subject for further investigations. Data are also

reconstructed outside the valid flow region. Hence, masking has to be applied similar to Tomo-PIV. Whereas data assimilation is used to maximize the spatial resolution for time-resolved data by using physical laws, a second way to increase the spatial resolution is accumulating the information of multiple time steps and retrieving temporal averages [Kähler et al. (2012a)]. Here, data binning of STB tracks is of great practical advantage over Tomo-PIV since bins are only defined as valid where particle tracks can be detected such that no complex masking has to be applied in this study. From the resulting temporal average over 1000 time steps also the relative pressure field is reconstructed, which exposes a sensible pressure gradient. Also the shorter processing time of STB and binning-based conversion to a regular grid compared to Tomo-PIV is an advantage of STB processing combined with data binning under these conditions. To the authors' knowledge, this is the first paper presenting STB applied to microscopic flows. Overall, it proves that STB is a powerful measurement method for three dimensional microscopic flow measurement.

References

Agüera N, Cafiero G, Astarita T, and Discetti S (2016) Ensemble 3D PTV for high resolution turbulent statistics. *Measurement Science and Technology* 27:124011

Cierpka C and Kähler CJ (2012) Particle imaging techniques for volumetric three-component (3D3C) velocity measurements in microfluidics. *Journal of Visualization* 15:1–31

Elsinga GE, Scarano F, Wieneke B, and van Oudheusden BW (2006) Tomographic particle image velocimetry. *Experiments in Fluids* 41:933–947

Jeon YJ, Müller M, Michaelis D, Pfeiffer K, and Wieneke B (2017) Boundary condition assignment for evaluating instantaneous pressure field from Time-resolved PIV. *ISPIV Conference* Session M1 on Monday 19th

Jeon YJ, Müller M, Michaelis D, and Wieneke B (2019) Data assimilation-based flow field reconstruction from particle tracks over multiple time steps. *ISPIV Conference*

Kähler CJ, Scharnowski S, and Cierpka C (2012a) On the resolution limit of digital particle image velocimetry. *Experiments in Fluids* 52:1629–1639

Kähler CJ, Scharnowski S, and Cierpka C (2012b) On the uncertainty of digital PIV and PTV near walls. *Experiments in Fluids* 52:1641–1656

Lynch KP and Scarano F (2015) An efficient and accurate approach to MTE-MART for time-resolved tomographic piv. *Experiments in Fluids* 56:66

Raffel M, Willert CE, Scarano F, Kähler CJ, Wereley ST, and Kompenhans J (2018) *Particle Image Velocimetry*. chapter Tracer Particles, page 39. Springer. 3rd edition

Schanz D, Gesemann S, and Schröder A (2016) Shake-The-Box: Lagrangian particle tracking at high particle image densities. *Experiments in Fluids* 57:70

Schanz D, Gesemann S, Schröder A, Wieneke B, and Novara M (2012) Non-uniform optical transfer functions in particle imaging: calibration and application to tomographic reconstruction. *Measurement Science and Technology* 24:024009

Schneiders JFG and Scarano F (2016) Dense velocity reconstruction from tomographic PTV with material derivatives. *Experiments in Fluids* 57:139

Westerweel J and Scarano F (2005) Universal outlier detection for PIV data. *Experiments in Fluids* 39:1096–1100

Wieneke B (2008) Volume self-calibration for 3D particle image velocimetry. *Experiments in Fluids* 45:549–556

Wieneke B (2018) Improvements for volume self-calibration. *Measurement Science and Technology* 29:084002